ELSEVIER

Journal of Structural Geology 29 (2007) 1781–1797

JOURNAL OF STRUCTURAL GEOLOGY

www.elsevier.com/locate/jsg

Structural insights into the early stages of exhumation along an orogen-scale detachment: The South Tibetan Detachment System, Dzakaa Chu section, Eastern Himalaya

John M. Cottle [a,*], Micah J. Jessup [b], Dennis L. Newell [c], Michael P. Searle [a], Richard D. Law [d], Matthew S.A. Horstwood [e]

[a] *Department of Earth Sciences, University of Oxford, Parks Road, Oxford OX1 3PR, UK*
[b] *Department of Earth and Planetary Sciences, University of Tennessee, Knoxville, TN 37969, USA*
[c] *Department of Geosciences, Virginia Tech., Blacksburg, VA 24061, USA*
[d] *Department of Earth and Planetary Sciences, University of New Mexico, Albuquerque, NM 87131, USA*
[e] *NERC Isotope Geosciences Laboratory, British Geological Survey, Keyworth, NG12 5GG, UK*

Received 22 January 2007; received in revised form 17 August 2007; accepted 23 August 2007
Available online 19 September 2007

Abstract

Structural transects through the South Tibetan Detachment system (STDS) in the Dzakaa Chu valley, Tibet reveal a ~1000-m thick, low-angle (<35°) zone of distributed ductile shear that displaces Paleozoic sediments over amphibolite facies gneisses, calc-mylonites and leucogranites of the Greater Himalayan Series (GHS). Within the shear zone, grain-size reduction with dynamic recrystallisation of quartz and growth of secondary phyllosilicates accommodated ductile deformation at elevated temperatures. Small-scale brittle normal faults and extensional shear veins overprint ductile features recording deformation at lower temperatures. Our structural data indicate that the Dzakaa Chu STDS records a progression from ductile- to brittle-deformation without development of a discrete detachment fault(s) that is common to many STDS sections. U(−Th)−Pb dating of post-kinematic leucogranites suggest that, in the lower part of the shear zone, mylonitic fabric development occurred prior to ~20 Ma. By integrating structural and geochronological evidences we propose that the Dzakaa Chu STDS represents a deeper structural position than elsewhere in the Himalaya and provides important insight into the early ductile exhumation of the GHS that was dominated by movement along a 1-km wide shear zone without discrete brittle detachments. These findings are an important step towards understanding the development of low-angle detachment fault systems active during continental collision.

Keywords: South Tibetan Detachment system; Shear zone; Himalaya; U−Th−Pb Geochronology

1. Introduction and regional geology

The South Tibetan Detachment system (STDS) is a top-down-to-the-north, low-angle normal fault system extending ~2500 km along the Himalayan orogen from Zanskar in NW India to Arunachal Pradesh in the NE India (Fig. 1). In southern Tibet, the STDS was first identified by Burg (1983) and Burg and Chen (1984) and subsequently described in detail by Burchfiel et al. (1992). This orogen-scale detachment separates low-grade Cambrian to mid-Eocene Tibetan Sedimentary sequence (TSS) rocks in its hanging wall above from Late Proterozoic units of footwall gneiss of the Greater Himalayan Series (GHS) below (Fig. 1; Burg, 1983; Burg et al., 1984; Searle, 1986; Herren, 1987; Burchfiel et al., 1992; Edwards et al., 1996; Hodges et al., 1996; Searle et al., 1997, 2003; Wu et al., 1998; Grujic et al., 2002; Godin, 2003; Godin et al., 1999, 2001).

Recognition of this large-scale, low-angle normal fault structure, bounding the upper margin of the high-grade anatectic and

* Corresponding author. Tel.: +44 1865 272054; fax: +44 1865 272072.
E-mail address: john.cottle@earth.ox.ac.uk (J.M. Cottle).

0191-8141/$ - see front matter © 2007 Elsevier Ltd. All rights reserved.
doi:10.1016/j.jsg.2007.08.007

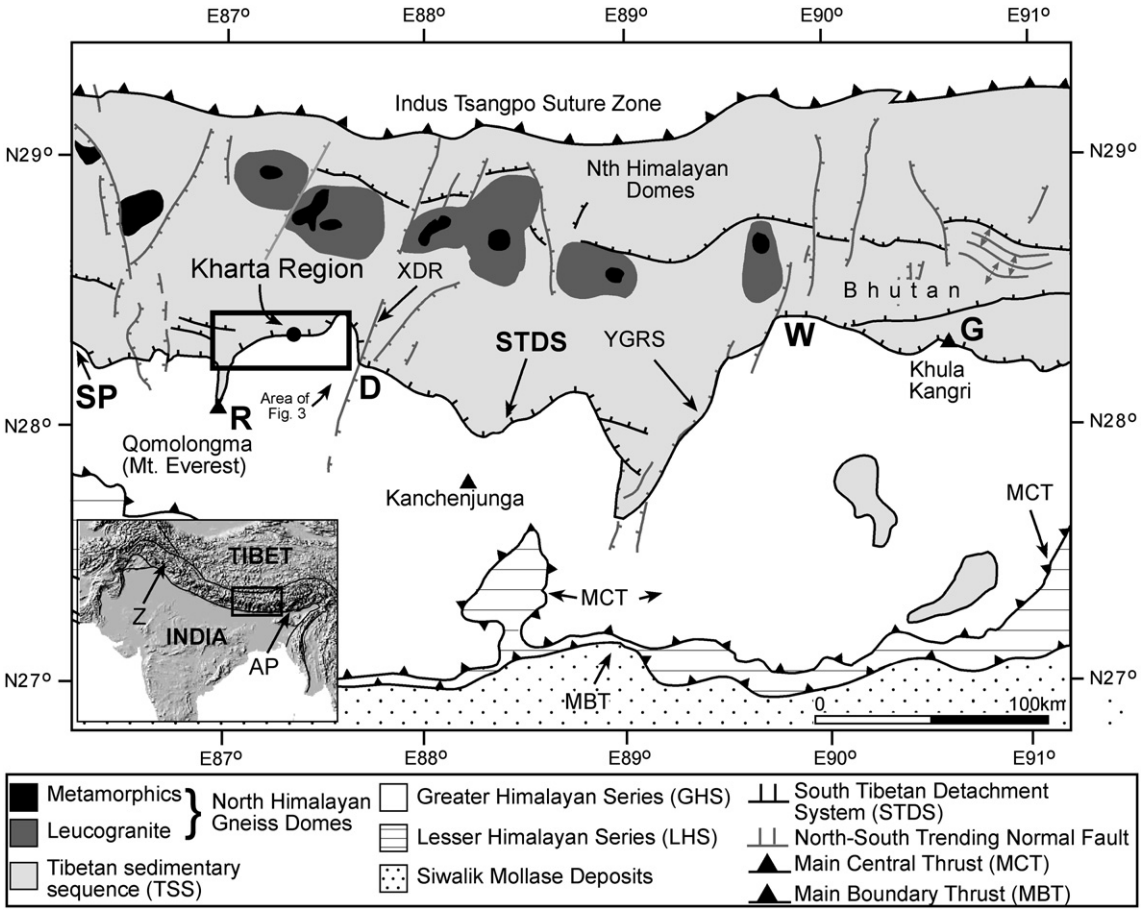

Fig. 1. Regional tectonic map of the Central Himalaya modified from Gansser (1983) and Burchfiel et al. (1992). The inset map shows its location within the Himalayan Orogen. The South Tibetan Detachment (STDS) marked by heavy ticked lines separates the Tibetan sedimentary sequence (TSS, light grey shading) in its hanging wall from the Greater Himalayan Series (GHS, white shading) in the footwall. Within the TSS, the North Himalayan domes are shown as leucogranite intrusions (black shading) surrounded by low–high-grade metamorphic rocks (dark grey shading). The Main Central Thrust (MCT) places the GHS over the Lesser Himalayan Series (LHS, horizontal line shading). South of the MCT the Main Boundary Thrust (MBT) thrusts the LHS over Siwalik molasse deposits. Grey ticked lines mark north–south trending Pliocene – recent normal faults. Locations referred to in the text: Z, Zanskar; AP, Arunachal Pradesh; SP, Shisha Pangma; R, Rongbuk (Everest); D, Dingyyê; W, Wagye La; G, Gonto la; YGRS, Yadong–Gulu rift system; XDR, Xainza-Dinggye rift.

metamorphic core of the Himalaya (GHS) was complemented by structural and geochronological studies of the Main Central Thrust (MCT); the south vergent thrust system that bounds the base of the GHS (Fig. 1). Several workers suggested that mid-Miocene thrusting on the MCT was concomitant with normal-sense movement on the STDS (Hubbard and Harrison, 1989; Searle and Rex, 1989; Burchfiel et al., 1992; Hodges et al., 1992, 1996). Although considerable debate over the evidence for synchronous movement on the MCT and STDS still exists (e.g., Murphy and Harrison, 1999), it is generally recognized that the MCT and STDS were, for at least part of their history, active contemporaneously. This development initiated a considerable shift in the Himalayan tectonic paradigm and gave rise to a variety of kinematic and thermal–mechanical models that attempted to explain the processes by which the mid-crustal GHS was extruded southward between these opposing-sense shear zones. Initial models involved a wedge geometry (Burchfiel and Royden, 1985; Royden and Burchfiel, 1987; Kündig, 1989; Burchfiel et al., 1992; Hodges et al., 1993; Grujic et al., 1996; Grasemann et al., 1999), in which the STDS and MCT merge at depth beneath the Tibetan Plateau. In many of these scenarios, extrusion was envisaged as being driven by gravitational collapse in response to the extreme topographic gradient along the southern margin of the Himalayas.

Further geological investigations (e.g., Grujic et al., 2002; Searle et al., 2003), re-interpretation of deep crustal seismic data and development of thermal–mechanical finite-element models (Beaumont et al., 2001, 2004, 2006; Jamieson et al., 2002, 2004, 2006) lead to the inception of the channel flow concept. In channel flow models, the GHS is viewed as a laterally continuous, low viscosity, mid-crustal channel that tunneled laterally southwards from beneath the Tibetan Plateau and eventually extruded towards the Himalayan range front. Horizontal gradients in lithostatic pressure between the Tibetan Plateau and the Himalayan front provided the driving force behind extrusion (Grujic et al. (1996). Exhumation of the GHS from mid-crustal depths to the surface is initiated by focused denudation along the high topographic relief that is present in the transition between the plateau and the orogenic front.

Although a general consensus on the importance of the STDS in the context of channel flow models and the Himalayan orogen exists; only a limited number of investigations have constrained the spatial and temporal variations in deformational processes that were responsible for movement along the STDS and their relationship to exhumation of the GHS (Law et al., 2004; Jessup et al., 2006a; Jessup et al., in press). To further compliment this approach to addressing these outstanding issues, we combine field- and lab-based structural analysis with new petrological and geochronological data to characterize the tectonic evolution of a well-exposed section of the STDS in the Dzakaa Chu valley near Kharta in southern Tibet (Figs. 1 and 2). These data provide important insights into the interaction between the progressive evolution of low-angle detachment faults, metamorphism and magmatism in collisional orogens and, more specifically, the Himalayan–Tibet orogenic system.

2. Location

The Dzakaa Chu valley lies ~60 km northeast of the Mount Everest Massif in southern Tibet (Fig. 2; Searle et al., 2003, 2006). The rugged topography and associated drainage systems expose a section of the STDS that separates the GHS below from lower Paleozoic to lower Mesozoic shelf carbonates of the TSS above (Burchfiel et al., 1992). We refer to this segment of the STDS as the Dzakaa Chu section. Here, the GHS is composed of upper amphibolite to granulite facies leucogneisses, metapelites, calc-silicates and minor marble that are intruded by a network of centimeter- to decimeter-thick crustal melt leucogranite dykes and sills. The volume-of-melt increases up structural section, with the immediate footwall of the STDS comprising up to 75% leucogranite. Immediately to the east of the Dzakaa Chu section, both tectonic units and the STDS are folded and displaced by the north-plunging Arun Antiform (a.k.a. Ama Drime Massif (ADM), Nyon Ri or Gyankar range) (Fig. 2) (Jessup et al., 2006b). To the east of the ADM, the Dinggye valley contains Xainza-Dinggye rift that extends north into the Tibetan Plateau (Fig. 1; Zhang and Lei, 2007). Burchfiel et al. (1992) suggest that the north–south striking detachment fault/shear zone system that bounds the eastern margin of the ADM, displaces the STDS by 20 km of right-lateral separation. By offsetting the STDS, these younger features provide compelling evidence that the STDS is inactive in this region.

The STDS in this region was originally identified and regionally mapped by Carosi et al. (1999) and Searle et al. (2003, 2006); however, prior to this investigation, details regarding the kinematics, timing and duration of movement on this segment of the fault system, its spatial and temporal relationship to slip on the STDS to the west in the Everest region, as well as its significance in the Himalayan orogen were lacking.

Forty-five kilometers southwest of the Dzakaa Chu, in the Everest (Rongbuk) region, the STDS is composed of two major detachments (Burchfiel et al., 1992; Carosi et al., 1998, 1999; Murphy and Harrison, 1999; Searle, 1999; Searle et al., 2003; Law et al., 2004; Jessup et al., 2006a) (Figs. 1–3). The upper brittle Qomolangma Detachment (QD), juxtaposes sedimentary rocks with carbonates and shales of the Everest

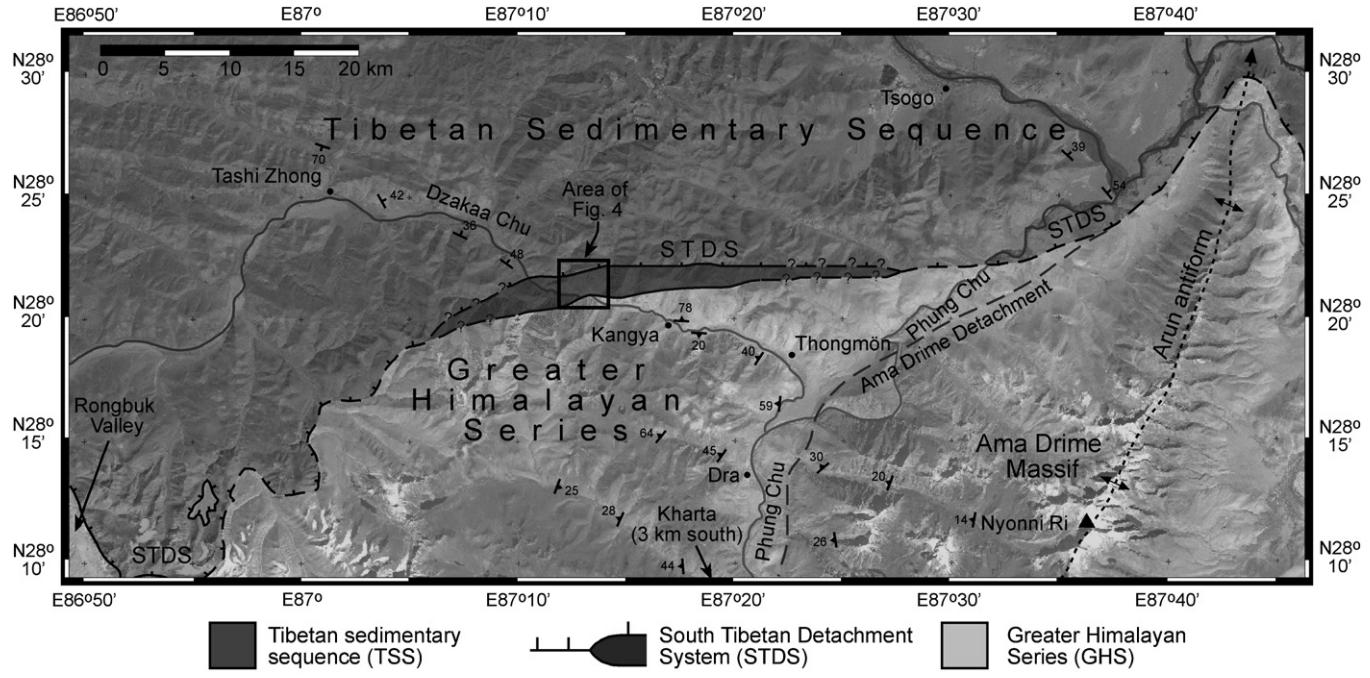

Fig. 2. Geological summary map of the Kharta Region (boxed area in Fig. 1) compiled from field observations and interpolation of ETM 7 + Landsat images. The STDS (medium grey shading and thick ticked lines) separates the GHS (lighter grey shading) in its footwall from the TSS (darker grey shading) in the hanging wall. Dashed lines indicate where the location of the STDS is known to ~±1 km. Question marks indicate areas where the nature of the STDS remains uncertain. Strike and dip symbols are foliation in the GHS and bedding in the TSS. The axial trace of the Arun Antiform is shown as a short-dashed line.

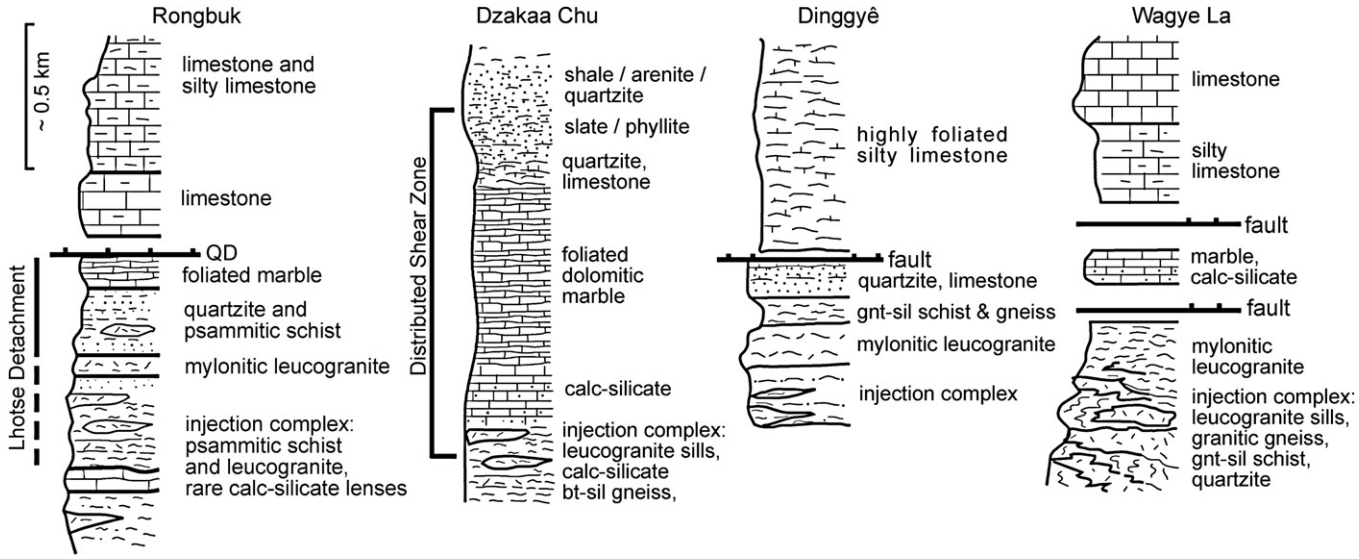

Fig. 3. Summary structural sections through the STDS at locations referred to in the text. Geographic locations of sections are shown in Fig. 1. The Rongbuk, Dingyyê and Wagye La sections are modified from Burchfiel et al. (1992).

Series below, while the second, structurally lower, Lhotse Detachment (LD), juxtaposes Everest Series with high-grade sillimanite–cordierite bearing gneisses injected by leucogranite sills and sheets. Newly recognized amphibolite facies rocks on both sides of the LD suggest a continuum in metamorphic grade, instead of a discrete break, characterises the LD (Jessup et al., 2004,2005,in press; Waters et al., 2006). Timing constraints on the STDS in the Everest area suggest that the upper brittle detachment was initiated at $\geq$16 Ma, while the lower ductile system was active at $\sim$17 Ma (Hodges et al., 1998; Murphy and Harrison, 1999; Searle et al., 2003).

Located 50 km to the east of the Dzakaa Chu, the Dingyyê section of the STDS (Figs. 1 and 3) (Burchfiel et al., 1992; Hodges et al., 1994) is marked by two low-angle normal faults, the Sa'er and Dingyyê Detachments. Differences in deformation style between the two faults led Burchfiel et al. (1992) to conclude that the lower Dingyyê detachment formed prior to the Sa'er detachment and was the principle structure that juxtaposed the GHS and TSS. Subsequent $^{40}Ar/^{39}Ar$ analyses by Hodges et al. (1994) suggested that the STDS at Dingyyê initiated at $\sim$16 Ma.

Approximately 150 km to the east of the Dzakaa Chu, lies the north–south trending Yadong–Gulu rift system (Fig. 1) (Armijo et al., 1986). On the eastern side of this structure, the STDS is offset $\sim$70 km northward. In these areas the STDS is similar in nature to that described from the Dingyyê and Everest regions in that it contains an older ductile shear zone that is truncated by a younger low-angle brittle detachment. The STDS consists of a detachment fault (the Gonto La Detachment) that separates mylonitised granites and gneisses of the GHS from the Tibetan metasedimentary sequence (Edwards et al., 1996) (Fig. 3). The $\sim$12 Ma Khula Kangri pluton (Edwards and Harrison, 1997) and a $\sim$12 Ma granite at Wayge La (Wu et al., 1998) are both truncated by the Gonto La Detachment (Fig. 3), implying that the STDS in this region of northern Bhutan was active after $\sim$12 Ma. A strand of the north–northeast-trending Yadong–Gulu rift system cuts the STDS and therefore movement on the STDS pre-dates the onset of east–west extension in Tibet at $\sim$8 Ma (Edwards et al., 1996).

3. Geological observations

Ten kilometers northwest of Kangya village, in the Dzakaa Chu river valley, the STDS is characterized by a $\sim$1000-m wide zone of distributed deformation that is recorded in both GHS and TSS rocks (Figs. 2–4). All rock types within the structurally lower section of the shear zone contain a pervasive mylonitic foliation and well-developed stretching lineation. Towards structurally higher positions, this zone of a penetrative mylonitic foliation and associated mineral stretching lineation transitions into a prominent slaty cleavage. This cleavage

Fig. 4. (A) Outcrop photograph of the lower section of the STDS. The exposures at the very top of the photograph contain the structurally lowest layers of quartzite (equivalent to the beds schematically displayed roughly in the middle of the zone in Fig. 4c). The photograph was taken looking approximately along strike (northeast). Dzakaa Chu River in the foreground. Photograph taken approximately 12 km northwest of Kangya village. (B) Photograph taken looking roughly down-dip (northwest) at the STDS section. Photograph taken approximately 10 km northwest of Kangya village. (C) Schematic cross section through the STDS section with the main lithotectonic units labeled. Fig. 4d–h are lower hemisphere, equal area stereonets of significant structural features within the Dzakaa Chu STDS section. (D) Composite stereonet of mylonitic foliation and mineral stretching lineation throughout the STDS zone. (E) Pi-poles to bedding (S_0), best fit pi-girdle to S_0 and fold hinges and hinge surfaces. These data summarize the structural observations in the hanging wall sediments over 3 km of section above the STDS. (F) Pi-poles to brittle extensional shear veins, enveloping surfaces of kink bands and normal faults within the shear zone. (G) Northeast verging fold hinges and hinge surfaces in the upper part of the STDS zone. (H) Pi-poles to bedding (S_0) in the immediate hanging wall of the STDS, also plotted for comparison is the mylonitic foliation within the STDS. Note that with decreasing elevation (down structural section) the orientation of bedding becomes closer to that of the mylonitic foliation within the shear zone. (I, J) Schematic three-dimensional block diagrams of features in the lower (I) and upper (J) sections of the STDS zone.

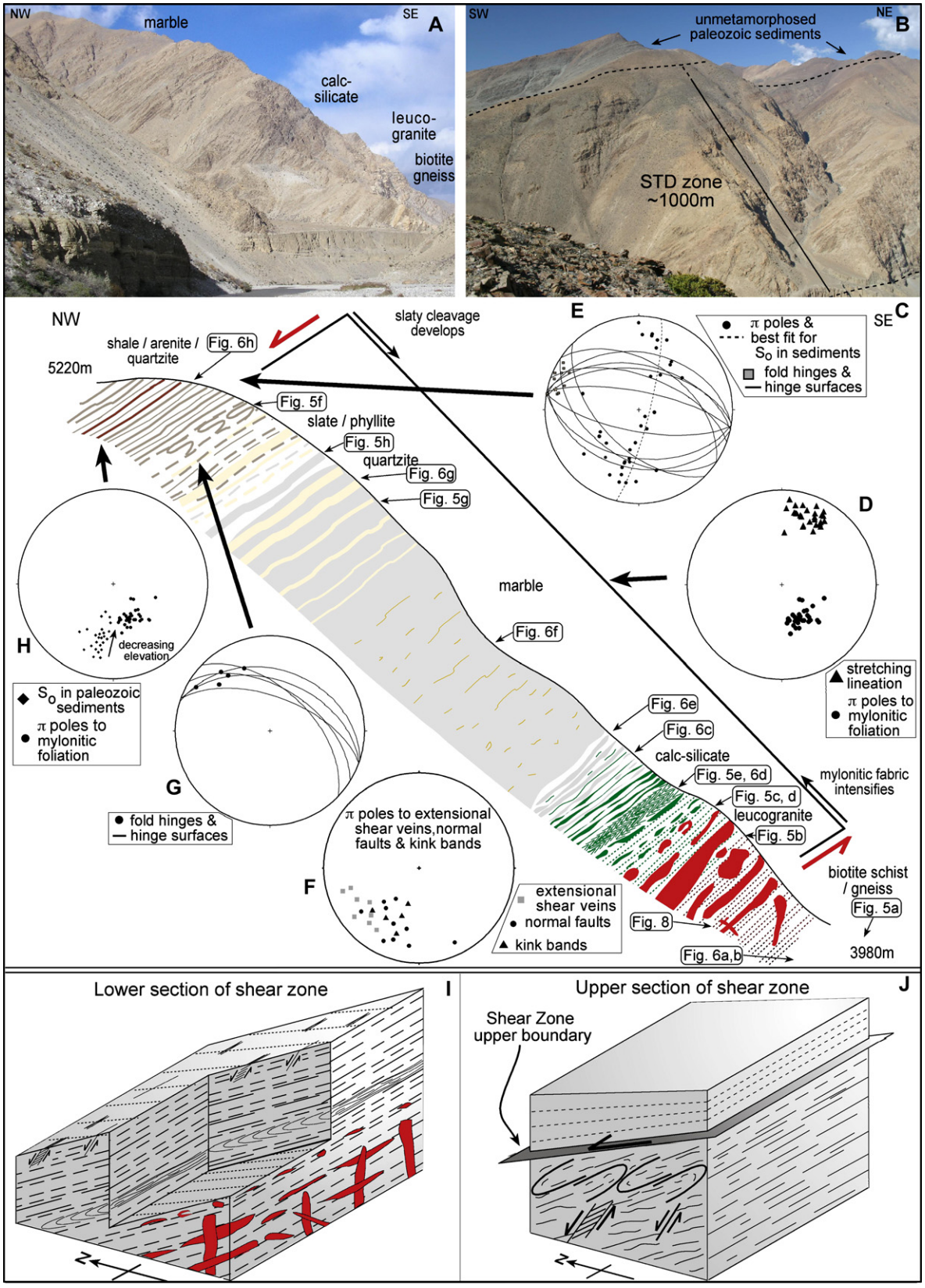
NW
marble
SE
A
calc-silicate
leuco-granite
biotite gneiss
SW
unmetamorphosed paleozoic sediments
NE
B
STD zone ~1000m
NW
shale / arenite / quartzite
Fig. 6h
5220m
Fig. 5f
slate / phyllite
Fig. 5h
quartzite
Fig. 6g
Fig. 5g
slaty cleavage develops
E
π poles & best fit for So in sediments
fold hinges & hinge surfaces
SE
C
D
marble
Fig. 6f
H
decreasing elevation
So in paleozoic sediments
π poles to mylonitic foliation
stretching lineation
π poles to mylonitic foliation
Fig. 6e
Fig. 6c
calc-silicate
Fig. 5e, 6d
Fig. 5c, d
leucogranite
Fig. 5b
mylonitic fabric intensifies
G
fold hinges & hinge surfaces
π poles to extensional shear veins,normal faults & kink bands
F
extensional shear veins
normal faults
kink bands
Fig. 8
Fig. 6a,b
biotite schist / gneiss
Fig. 5a
3980m
Lower section of shear zone
I
Upper section of shear zone
J
Shear Zone upper boundary
Z
Z

persists to the upper margin of the shear zone where it grades structurally up into undeformed and unmetamorphosed TSS hanging wall rocks. Well-foliated amphibolite facies Bt + Kfs + Pl ± Sil (abbreviations after Kretz, 1983) schist and gneiss, comparable to the Neoproterozoic Rongbuk Formation of Yin and Kuo (1978) in the Everest area are exposed in the structurally lowest outcrops of this section. Towards structurally higher positions, these gneisses and schists grade into a ~120-m thick section of interlayered calc-silicate and calc-mylonite (Fig. 4) with the assemblage Qtz, Ca-Plg + Bt + Di + Cal + Hbl ± Ep ± Ttn ± Kfs. Within these larger units, 10–50 cm thick dark green or black compositional banding (Bt + Hbl + Di + Ep) is common.

On the basis of crosscutting relationships, at least three generations of dykes, sills and anastamosing networks of two-mica and garnet–tourmaline leucogranite intrude the biotite gneiss and calc-silicate units (Figs. 4c, 5b). Boudinaged leucogranites form pods and stringers that are present in the middle section of the calc-silicate unit (Fig. 5c) and are occasionally folded (Fig. 5d). The occurrence of granitic bodies decreases rapidly towards the structurally highest section of the calc-silicate unit (Figs. 3, 4c) and does not appear to crosscut the entire STDS section.

Structurally overlying, and in gradational contact with, the calc-silicates is a 250-m thick section of fine-grained marble containing calcite (~30 to 120 μm in size) + Dol + Di ± Qtz ± phyllosilicate(s). Dolomitic horizons and alignment of elongate diopside porphyroclasts and quartz–white mica rich layers define a prominent foliation.

The marble grades structurally upwards into a sequence of impure quartzites, slate and phyllites (Fig. 4c) that preserve decimeter-scale, tight upright folds and an associated axial planar cleavage (Figs. 4e, g, 5f). Over this ~200-m thick structural section, the axial planar cleavage becomes progressively more difficult to define as the rocks grade upward into a sequence of essentially undeformed interlayered shales, fossiliferous siltstones, quartz arenites, conglomerates and red-beds (Fig. 4h). Although depositional age constraints on these rocks are absent, based on the age of similar lithologies present at structurally equivalent horizons above the STDS at other localities (Burchfiel et al., 1992), we suggest that these rocks are probably Ordovician in age.

3.1. Macro-structure

The fabric in the lower most exposed section of the shear zone is associated with the mineral assemblage Qtz + Pl + Kfs + Bt ± Sil ± Grt (Figs. 5a, b, 6a, b). Although we use the term 'S_1' foliation as a starting point for the following discussion, it does not preclude the presence of an earlier, unidentified foliation; nor do we intend to imply either protracted or discrete fabric forming events with this nomenclature. Elongate quartz ribbons and aligned biotite define the foliation (S_1), while the lineation (L_1) is defined by aligned fibrolite and biotite (Figs. 5a, b, 6a, b). Within the lower part of the shear zone, S_1 is transposed into a mylonitic foliation (S_2), defined by aligned quartz, biotite and amphibole, that strikes northeast (045°–074°) and dips (30°–40°) northwest (Fig. 4d). An associated mineral and stretching lineation defined by elongate biotite (L_2) trends north–northeast (010°–034°, mean of 024°) and plunges gently (10°–35°, mean 22°) (Fig. 4d). Mesoscopic tight to isoclinal F_2 folds are well developed in the calc-silicate units that structurally overlie the high-grade gneiss exposed at the base of the section (Fig. 5e). Small (>30 cm) leucogranite bodies occur as boudinaged inclusions within calc-silicate layers and are also folded on the meter-scale (Figs. 4c, 5c, d). At still structurally higher positions, within the phyllite/slate units, northeast verging decimeter-scale folds and an associated axial planar cleavage are well developed (Fig. 5f). The folds have gently north–northwest plunging hinges (~26° towards 318°) and axial planes (~296°, 35–60°NE) (Fig. 4g). Limited evidence for a pressure solution cleavage exists in the form of axial planar calcite stylolites in more calcareous rocks within the upper most section of the shear zone. A several hundred meter wide gradation exists between rocks within the upper part of the ductile shear zone with a pervasively transposed fabric (S_2) and those in the hanging wall that lack evidence for significant deformation and fabric development, instead retaining their original S_0 bedding (Fig. 4e, h).

Late-stage, northwest striking, steeply northeast dipping (57°–77°) brittle features overprint the ductile fabric throughout the shear zone (Fig. 4f). Quartz/carbonate-filled tension gashes, extensional shear veins and Riedel fractures are common and ubiquitously display top-to-the-northeast, normal-sense displacement as indicated by fracture opening direction and warping of foliation. Meter- to decimeter-scale north dipping brittle faults containing 1–5 cm thick cataclasite zones are also common. During two detailed structural transects, we found no evidence for a discrete detachment fault subparallel to the pervasive S_2 shear fabric that would be capable of accommodating large amounts of brittle displacement as in Rongbuk valley or other sections of the STDS along orogenic strike (Burchfiel et al., 1992; Carosi et al., 1998, 1999; Searle, 1999; Searle et al., 2003). Instead, we interpret this segment of the STDS to represent a ~1000 m wide zone of distributed ductile deformation affecting both GHS and TSS rocks that was subsequently overprinted at lower temperatures by small-scale, steeply dipping brittle features.

3.2. Micro-structure

At the deepest structural level of the transect, aligned quartz and feldspar define the main shear fabric (S_1). Polygonal quartz grains with small strain-free subgrains along grain boundaries indicate a component of subgrain rotation during dynamic recrystallisation of quartz within Regime 3 of Hirth and Tullis (1992) and suggest that deformation occurred at temperatures of >530 °C (Stipp et al., 2002). Feldspar grains are flattened, largely strain-free and often contain subgrains, suggesting that the formation of S_1 was associated with high temperature dynamic recrystallisation of feldspar (Figs. 5a, 6a, b) (Tullis and Yund, 1992; Fitzgerald and Stunitz, 1993). In these rocks, as previously documented in Rongbuk valley

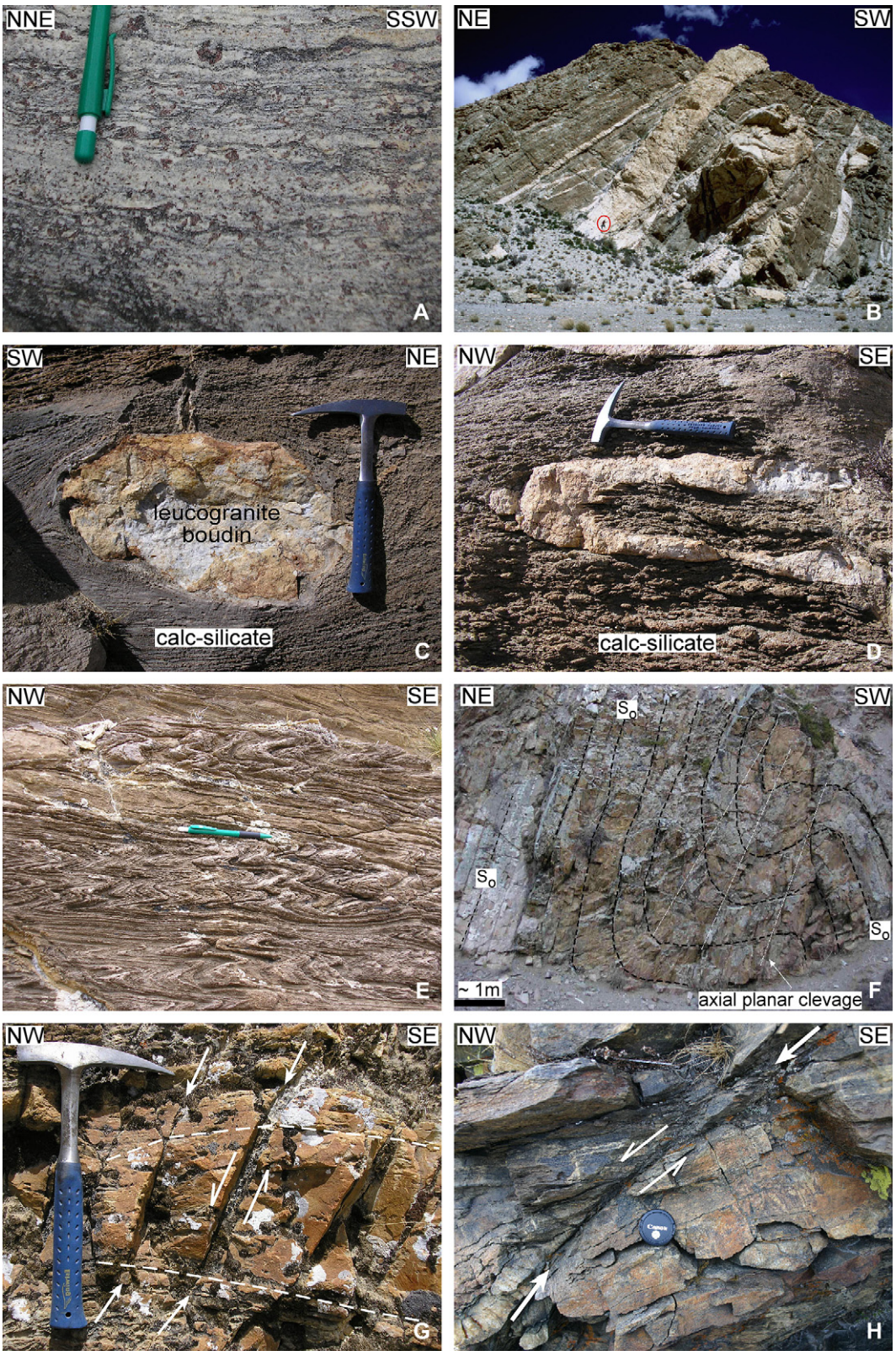

Fig. 5. Outcrop photographs of lithologies and macro-structural features within STDS zone. The approximate locations of Fig. 5a–h are shown on Fig. 4c. (A) Typical outcrop appearance of Gnt–Bt–Sil migmatitic gneiss in the upper kilometer of the GHS beneath the STDS footwall. (B) Outcrop photograph of sills and networks of leucogranites in the immediate footwall of the STDS. Note Geologist for scale. The outcrop illustrated in Fig. 5 (see below) is located at the lower-right side of this photograph. (C) Boudinaged and (D) folded leucogranite pods within the lower part of the STDS zone. These are the structurally highest leucogranites and occur within the upper mylonitic calc-silicate unit. The host lithologies represent a transition zone between hornblende–biotite gneiss and calc-silicate. (E) North-verging centimeter-scale tight to isoclinal folds in upper section of calc-silicate unit. (F) Northeast verging decimeter-scale folds in phyllite/slate units in the upper part of the STDS zone. Note the development of an axial planar cleavage in the fold hinge. (G) Quartz–calcite filled extensional shear veins offsetting foliation in marble. (H) Brittle normal fault in phyllite unit, apparent dip-slip separation is $\sim$5 m.

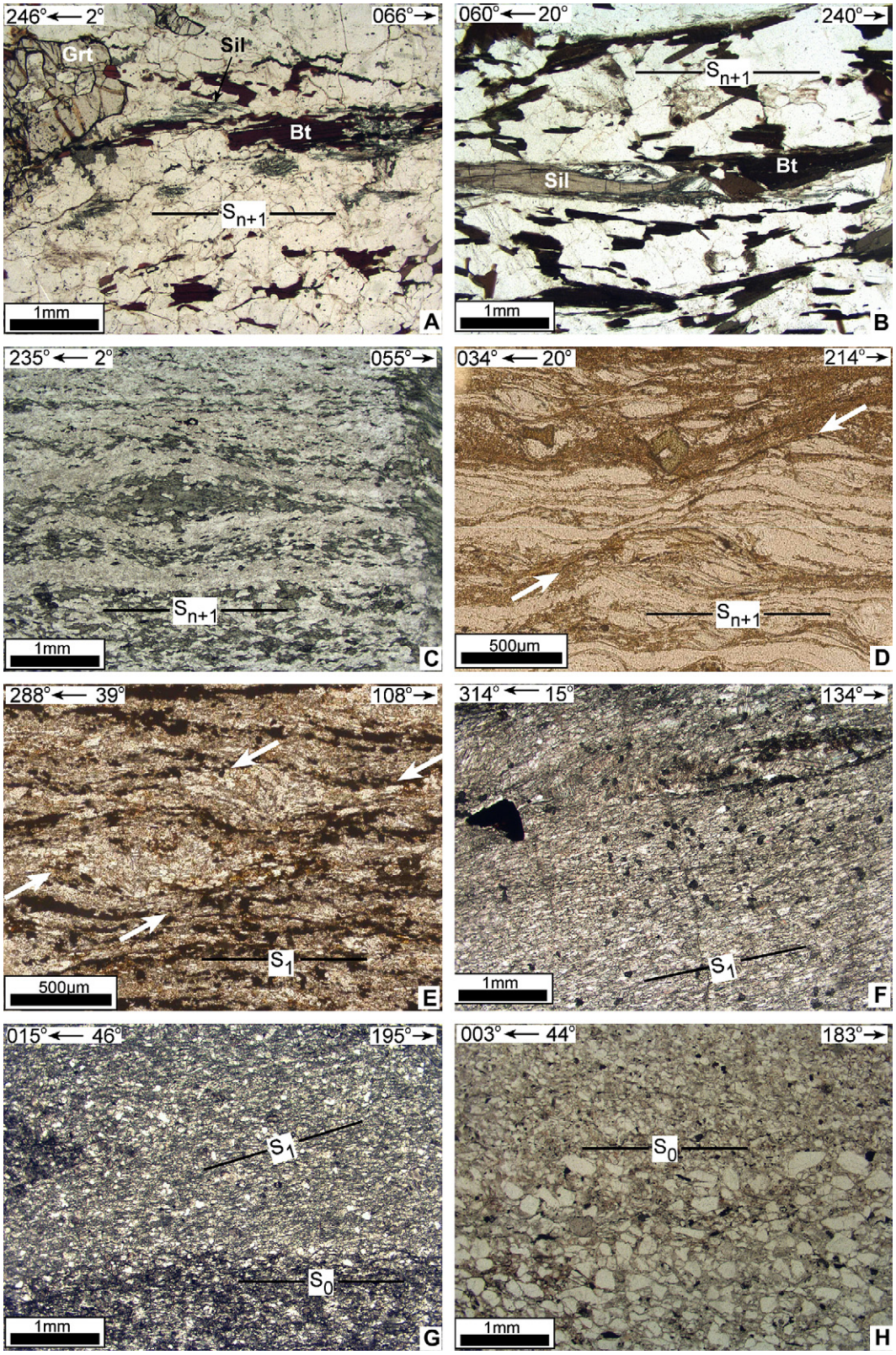
246° ← 2°
066° →
Grt
Sil
Bt
S_{n+1}
1mm
A
060° ← 20°
240° →
S_{n+1}
Sil
Bt
1mm
B
235° ← 2°
055° →
S_{n+1}
1mm
C
034° ← 20°
214° →
S_{n+1}
500μm
D
288° ← 39°
108° →
S_1
500μm
E
314° ← 15°
134° →
S_1
1mm
F
015° ← 46°
195° →
S_1
S_0
1mm
G
003° ← 44°
183° →
S_0
1mm
H

by Law et al. (2004), fibrolite that is drawn into extensional shear bands is interpreted to be syn-kinematic and suggests that deformation occurred at, or close to, the sillimanite stability field (>500 °C). A component of bulk pure shear coaxial flow is suggested by ubiquitous conjugate sets of shear bands with top–down to the south–southwest or top–down to the north–northeast sense of shear. These observations are consistent with those made by Law et al. (2004) and Jessup et al. (2006a) in the Rongbuk Formation in the Everest section.

Towards structurally higher positions, the pervasive mylonitic fabric (S_2) that overprints the higher temperature regional gneissic fabric (S_1) dominates the shear zone. Feldspar within this zone displays undulose extinction along with development of deformation twins and new subgrains along grain boundaries, indicating deformation temperatures of >450–500 °C (Tullis and Yund, 1992; Fitzgerald and Stunitz, 1993). The presence of strain-free subgrains and relicts of grain boundaries that are defined by inclusion trails in quartz, suggest that quartz recrystallisation was accommodated by subgrain formation and grain boundary migration that are characteristic of Regimes 2–3 of Hirth and Tullis (1992) and indicate deformation temperatures in the 490–530 °C range (Stipp et al., 2002; their Fig. 2). Mylonitic deformation in these rocks was also associated with growth of phyllosilicates and/or amphibole (Fig. 6c–e) that defines the strong planar fabric to the rocks. Micro-scale top–down to the north–northeast extensional shear bands (Fig. 6d, e), asymmetric forward rotated σ-type porphyroclasts and mica fish consistently record top–down to the north–northeast sense of shear.

The pervasive mylonitic fabric continues to dominate the shear zone within a marble unit that overlies the calc-silicates (Fig. 4c). Here, dolomitic horizons, that we interpret as compositional layering, are transposed into a new, oblique fabric (S_2), defined by elongate calcite crystals, discontinuous pods of coarser calcite and to a lesser extent elongate quartz (Fig. 6f, g). Quartz and calcite grains display undulose extinction. Calcite lacks a strong crystallographic preferred orientation (CPO) but displays prominent Type II thick twins (Burkhard, 1993), suggesting deformation at $T > 200$ °C (Ferrill et al., 2004). Recrystallisation and growth of rare small calcite grains occurred along grain boundaries. Phyllosilicates, predominantly white mica, define shear bands with a similar orientation and same sense of shear as those in the structurally lower part of the shear zone.

In the overlying slate, phyllite, shale, arenite and quartzite (Fig. 4c), the transposed fabric (S_2) is less well defined at a micro-structural level; although some (slate and phyllite) units still preserve a spaced cleavage defined by biotite and/or chlorite that is oblique to S_0 and axial planar to north-verging decimeter-scale tight folds (Fig. 5f). At the very highest levels, a marked transition occurs over ~30 m of structural thickness that defines the upper limit to penetrative deformation and fabric development in the shear zone. In the lower part of the transition zone, rocks contain a weak fabric, defined by preferred alignment of phyllosilicates and contain evidence of deformation at moderate-low temperatures, including brittle fracturing of quartz, pressure solution development in calcite and deformation twinning in dolomite and calcite (Fig. 6g). In the upper part of the transition zone at the top of the transect, rocks show no evidence of cleavage development or growth of metamorphic phyllosilicates and preserve sedimentary structures such as graded bedding (Fig. 6h), cross-beds and fine-scale sedimentary laminations.

4. Displacement estimates

Quantitative estimates of minimum normal-sense dip-slip displacement have been reported for several segments of the STDS. In Zanskar (Fig. 1), based on the juxtaposition of estimated P–T conditions from high-grade metamorphic rocks in the footwall with essentially unmetamorphosed hanging wall TSS rocks, normal-sense displacement on the STDS has been estimated at 40–60 km (Dèzes et al., 1999; Searle et al., 1999; Walker et al., 1999; Robyr et al., 2002). Using a similar approach in the Shisha Pangma area of southern Tibet (Fig. 1), Searle et al. (1997) argued that movement along the STDS has eliminated a minimum of 10–12 km of structural section. Using the offset of rocks in hanging wall and footwall from the summit of Everest to the northern limit of Rongbuk valley, a minimum dip-slip displacement was initially estimated at 35–40 km (Burchfiel et al., 1992; Hodges et al., 1998). Subsequent work (Searle et al., 2002) suggests that displacement may have exceeded 90–100 km. In the eastern Himalaya of Bhutan, structural overlap between the Tethyan sedimentary rocks and the GHS implies a minimum normal-sense displacement of >140 km (Grujic et al., 2002). On the Tibet–Bhutan border in the Gonto La area Edwards et al. (1996) suggested that the Gonto La detachment accommodated a minimum of 15 km of displacement.

Preliminary thermobarometric analyses using garnet–biotite thermometry (employing the model of Bhattacharya et al., 1992) and garnet–plagioclase–aluminosilicate–quartz barometry (using the thermodynamic data set of Powell and Holland, 1988) on samples collected from the lower most

Fig. 6. Plane polarized light photomicrographs of samples from the Dzakaa Chu STDS; micrographs A–F are from sections cut perpendicular to foliation and parallel to lineation while (G) and (H) are cut perpendicular to bedding. Plunge and trend of lineation are shown for samples A–F, and orientation of bedding (S_0) for samples (G) and (H). The approximate locations of Fig. 6a–h are shown on Fig. 4c. (A) Greater Himalayan Series Gt–Bt–Sil gneiss from ~600 m beneath the STDS (sample KA68): Bt and Sil define a gneissic fabric. (B) Greater Himalayan Series Bt–Sil gneiss from ~300 m beneath the STDS (sample KA66): Bt and Sil define a strong planar fabric. (C) Hornblende-bearing calc-silicate from lower part of shear zone (sample KA93): showing a well developed planar fabric defined by aligned amphibole. A late-stage sub-vertical actinolite vein at the extreme right of photo cuts the fabric. (D) Biotite-rich calc-silicate (sample KA97): well-developed normal-sense shear bands (arrowed). (E) Foliated calc-silicate (sample KA93) the foliation is defined by biotite and feldspar with localized development of closely spaced top–down to the north extensional shear bands (arrowed). (F) Foliated marble (sample KA70): recrystallised calcite defining a well-developed foliation (S_1). (G) Marble (sample KA91): bedding (S_0) defined by dolomitic horizons (darker layer at bottom), transposed into a weakly developed spaced cleavage (S_1). (H) Quartz arenite from the hanging wall of the STDS, (sample KA77): showing right-way-up, graded bedding.

exposed section of the Dzakaa Chu section yield P–T estimates of 705 ± 30 °C and 7.8 ± 1.5 kbar. Assuming a lithostatic gradient of 3.5 km/kbar^{-1} (based on a crustal density of 2800 kg m^{-3}) and originally horizontal isograds at depth beneath the STDS, this pressure suggests these rocks equilibrated at depths of between ~22 and 33 km.

To translate the depths into an approximate horizontal displacement estimate a simple trigonometric model was constructed (Fig. 7). This model makes four main assumptions as outlined by Searle et al. (2003): (1) minimal erosion north of the STDS since the mid-Miocene; (2) average surface elevation of Southern Tibet prior to fault initiation was approximately 5 km, i.e., the same as it is now; (3) hanging wall remained fixed, with displacement entirely attributable to the southward motion of the footwall (i.e., passive roof fault); and (4) STDS has a constant dip which does not change significantly at depth. Although the first two points are the subject of considerable debate concerning other aspects of Himalayan tectonics, their impact on the displacement estimates is relatively small. For example, increasing the elevation of the Tibetan Plateau by 1 km decreases the displacement estimate by less than 0.6 km. The third assumption is also a matter of controversy, but several workers (e.g., Walker et al., 1999; Vannay and Grasemann, 2001; Searle et al., 2003; Law et al., 2004; Jessup et al., 2006a) have argued that the STDS acted as a passive roof fault to the southward extruding footwall GHS, providing support for the notion that the hanging wall remained fixed relative to the footwall. Further complications arise when the third assumption is applied to the Dzakaa Chu shear zone where hanging wall and footwall rocks cannot be distinguished. Variations in the last assumption, the dip of the STDS, have the most significant effect on displacement estimates. We cautiously use two end-member values to constrain minimum and maximum displacement estimates so that these results can be compared with existing displacement estimates on the STDS (Fig. 7). Taking the average local dip of the mylonitic foliation in the Dzakaa Chu section, of 32°, yields a horizontal displacement of GHS footwall rocks of ~50 km (Fig. 7). Given that we are unable to discount the possibility that the STDS has undergone post-movement rotation – particularly with its close proximity to the ADM – we suggest that this value represents a minimum displacement estimate. An estimate of the maximum displacement can be made by taking a 'regional' dip of the STDS of ~15°, as identified beneath the southern margin of the Tibetan Plateau in project INDEPTH deep seismic profiles (Nelson et al., 1996). This indicates that GHS footwall rocks may have been displaced southward beneath the STDS by as much as ~80 to 120 km (Fig. 7).

5. Timing of deformation – U–Th–Pb monazite geochronology

To constrain the timing and duration of ductile fabric development within the Dzakaa Chu section of the STDS, three samples of lecuogranite were collected from the lower part of the shear zone (Figs. 4c and 8). At this location three generations of leucogranites are clearly visible. The oldest leucogranite (KG43) is a foliation-parallel sill that displays a weakly developed biotite–muscovite foliation and mineral stretching lineation parallel to that of the host metamorphic rocks. We infer this to be pre- to syn-kinematic with respect to development of the mylonitic foliation in the shear zone. The host metamorphic rocks and the leucogranite KG43 are truncated by an post-kinematic dyke (KG47) which in turn is cross-cut by a foliation-parallel sill (KG45). Unfortunately datable minerals could only be extracted from KG45 and KG47.

Samples were analysed for U–Th–Pb isotopes by Laser Ablation Multi-Collector Inductively Coupled Mass

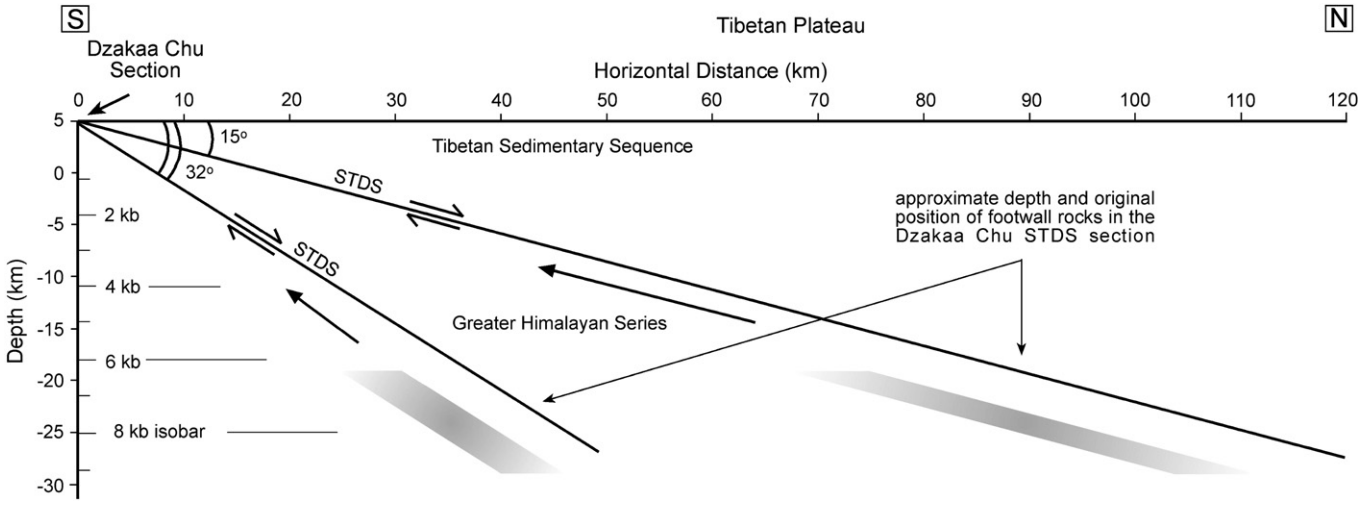

Fig. 7. Trigonometric model used to calculate the apparent displacement along the STDS in the Dzakaa Chu section. Pressure estimates for rocks in the immediate footwall of the STDS range from 6.3 to 9.3 kbar, equating to equilibration at depths of between ~22 and 32 km (the original pre-displacement position of these rocks is shown by the grey shading). Using a 32° dip of the STDS (average dip of local mylonitic foliation) gives a horizontal displacement of GHS footwall rocks beneath the STDS of ~50 km. Taking a 'regional' dip of the STDS of ~15°, as identified beneath the southern margin of the Tibetan Plateau in project INDEPTH deep seismic profiles (Nelson et al., 1996) yields a horizontal displacement of 80–120 km. See text for details of the assumptions made in this model.

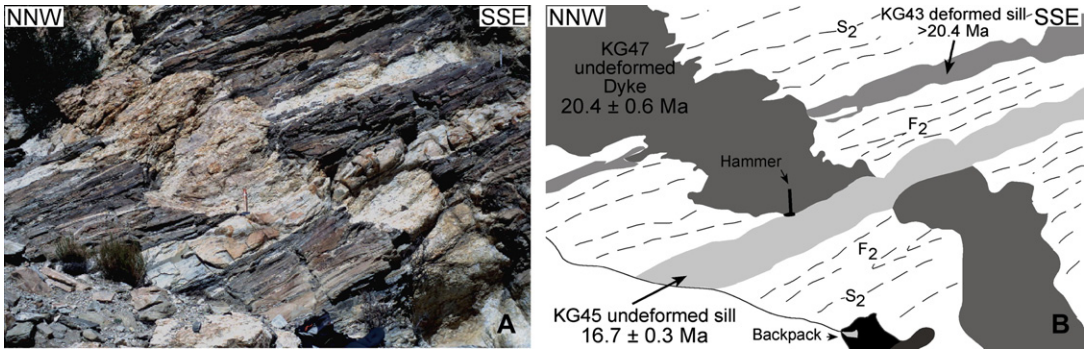

Fig. 8. Photograph (A) and interpretation (B) of the outcrop (N28° 20.788′ E87° 13.884′; elevation: 4005 m.a.sl) within the lower part of the STDS zone showing locations of leucogranite samples KG45 and KG47 analysed for U–Th–Pb geochronology. The location of this outcrop is shown on Fig. 4c. Photograph looking east northeast. Note hammer (centre) and backpack (lower-right) for scale.

Spectrometry (LA-MC-ICPMS) at the National Isotope Geoscience Laboratories (NIGL) Keyworth using a pseudo-simultaneous acquisition method modified from Horstwood et al. (2003). Data are presented in Table 1, and the full analytical methodology and petrographic descriptions of analysed monazites are given in Appendix 1.

5.1. Undeformed dyke KG47

5.1.1. Sample description

KG47 is a medium-grained two-mica tourmaline leucogranite dyke with accessory phases dominated by zircon and monazite. The dyke is oriented almost orthogonal to the foliation of the host metamorphic rocks (Fig. 8). On the macroscale the dyke shows no evidence of an internal fabric or having undergone significant deformation or sub-solidus recrystallisation. This is confirmed by micro-structural observations, which show a lack of deformation fabric, retaining its original igneous texture. The discordant relationship to the host rock foliation and undeformed nature of KG47 indicate that its emplacement post-dates ductile deformation and associated fabric development at this structural level within the STDS shear zone. In short, it provides a means to assess the minimum age of ductile deformation at the lowest structural level of the STDS.

5.1.2. KG47 monazite U–Th–Pb data

A total of nine 35 μm spot analyses were obtained from seven monazite grains (Table 1). The analyses define a reversely discordant sub-vertical linear array on a $^{208}Pb^*/^{232}Th$–$^{206}Pb^*/^{238}U$ concordia plot (where Pb* represents the radiogenic Pb, the total Pb minus common-Pb) (Fig. 9a). We interpret the reverse discordance observed in these grains to reflect incorporation of excess ^{230}Th during crystallisation, leading to an excess of ^{206}Pb, a phenomenon commonly observed in young monazites (Schärer, 1984; Parrish, 1990). With this in mind we take the $^{208}Pb^*/^{232}Th$ dates as the most reliable estimates of the ages of these grains. All the nine analyses give a weighted mean age of 20.4 ± 0.6 Ma with an MSWD (Wendt and Carl, 1991) of 1.7. Analyses of both core and rim domains on the several grains (Appendix 1) reveals that within the resolution of the LA-MC-ICPMS analytical technique there is no evidence of protracted accessory phase growth.

5.2. Undeformed sill KG45

5.2.1. Sample description

KG45 is a medium-grained biotite leucogranite collected from a ~60 cm thick sill oriented parallel to the foliation in the host metamorphic rocks in the lower part of the STDS zone (Fig. 8). The sill has a thin, 2–5 cm thick finer grained 'chilled' margin with a coarser core. It retains its primary igneous texture with no petrographic evidence of sub-solidus recrystallisation. Fig. 8 shows that KG45 crosscuts the dyke KG47 and is therefore younger than KG47, providing an external check of the age of the latter.

5.2.2. KG45 Monazite U–Th–Pb data

A total of sixteen, 35 μm spot analyses on 11 monazite grains were obtained from KG45. Data are compiled in Table 1 and presented in Fig. 8b. Eleven of the analyses define a reversely discordant vertical linear array on a common-lead corrected $^{208}Pb/^{232}Th$–$^{206}Pb/^{238}U$ concordia plot and define a weighted mean age of 16.7 ± 0.3 Ma with an MSWD (Wendt and Carl, 1991) of 1.07. This age is interpreted to reflect the timing of crystallisation of the sill. The remaining five analyses plot on, or slightly above concordia and have ages between ~5 and 12 million years older than the main population. We interpret these older age components to be the result of inheritance from multiple discrete age sources (see Appendix 1 for further details).

6. Discussion

6.1. Timing of deformation

New age constraints presented here indicate that strain accumulation and associated ductile fabric development in the lower part of the shear zone occurred prior to 20.4 ± 0.6 Ma, the emplacement age of the leucogranite dyke (KG47). Data presented here contrasts with the Everest and Wayge La/Gonto

Table 1
U–Th–Pb isotope data for analysed monazites

Name	Th (ppm)[a]	Th/U[b]	Uncorrected isotopic ratios				Uncorrected ages				Common-Pb corrected isotopic ratios[d]					Common-Pb corrected ages			
			$^{206}Pb^{c}/^{238}U$	2σ%	$^{208}Pb/^{232}Th$	2σ%	$^{206}Pb/^{238}U$	2σ (Ma)	$^{208}Pb/^{232}Th$	2σ (Ma)	f206%[c]	$^{206}Pb/^{238}U$	2σ%	$^{208}Pb/^{232}Th$	2σ%	$^{206}Pb/^{238}U$	2σ (Ma)	$^{208}Pb/^{232}Th$	2σ (Ma)
Sample KG45 monazite																			
014-1	28650	8.0	0.0035	1.915	0.0011	2.095	22.6	0.4	22.4	0.5	3.42	0.0033	5.840	0.0011	4.384	21.5	1.3	22.1	1.0
039-1	38436	10.0	0.0030	2.162	0.0008	2.135	19.4	0.4	16.7	0.4	−2.43	0.0032	6.659	0.0008	4.624	20.7	1.4	17.0	0.8
039-2	14385	4.1	0.0026	2.068	0.0008	2.520	16.8	0.3	17.1	0.4	−5.62	0.0027	9.412	0.0009	11.467	17.2	1.6	17.8	2.0
042-1	39913	5.7	0.0040	1.778	0.0013	2.147	26.0	0.5	26.6	0.6	2.78	0.0040	2.836	0.0013	3.138	25.5	0.7	25.7	0.8
042-2	41752	5.7	0.0041	1.682	0.0013	2.347	26.4	0.4	25.8	0.6	0.24	0.0041	3.580	0.0013	3.105	26.5	1.0	25.8	0.8
013-1	26297	13.0	0.0027	2.756	0.0008	2.469	17.5	0.5	16.6	0.4	−6.44	0.0027	17.708	0.0008	8.730	17.1	3.0	17.0	1.5
011-1	36278	16.9	0.0028	2.708	0.0009	2.345	17.8	0.5	17.2	0.4	5.49	0.0029	15.559	0.0008	5.913	18.4	2.9	17.0	1.0
040-1	49775	20.2	0.0034	2.394	0.0009	2.390	21.6	0.5	17.3	0.4	3.40	0.0035	9.987	0.0009	4.221	22.5	2.2	17.3	0.7
041-1	41429	17.9	0.0038	2.660	0.0008	2.483	24.2	0.6	16.7	0.4	4.69	0.0037	11.020	0.0008	5.798	24.0	2.6	16.4	1.0
003-1	30634	15.3	0.0035	3.411	0.0008	2.844	22.6	0.8	17.1	0.5	4.16	0.0038	15.760	0.0009	8.421	24.3	3.8	17.2	1.4
003-2	35670	17.4	0.0035	2.477	0.0009	2.558	22.4	0.6	17.9	0.5	13.27	0.0029	11.600	0.0008	5.028	18.7	2.2	16.4	0.8
001-1	31385	19.4	0.0027	3.748	0.0008	2.498	17.5	0.7	16.5	0.4	6.79	0.0027	20.009	0.0008	7.326	17.1	3.4	16.1	1.2
043-1	31301	9.6	0.0043	5.268	0.0012	2.956	27.5	1.5	23.5	0.7	1.61	0.0043	7.054	0.0012	4.091	27.7	2.0	23.4	1.0
042-3	30105	4.9	0.0044	5.257	0.0015	3.271	28.5	1.5	29.4	1.0	1.72	0.0044	6.178	0.0014	4.625	28.2	1.7	28.6	1.3
005-1	36232	18.0	0.0035	6.384	0.0008	2.984	22.6	1.4	16.8	0.5	7.72	0.0033	12.771	0.0008	4.433	21.2	2.7	16.4	0.7
007-2	23998	12.3	0.0035	5.343	0.0009	3.137	22.4	1.2	17.8	0.6	13.97	0.0027	13.128	0.0008	6.726	17.5	2.3	15.8	1.1
Sample KG47 monazite																			
003-2	22297	6.6	0.0092	22.480	0.0011	5.641	59.0	13.3	22.2	1.3	4.98	0.0091	23.610	0.0011	7.130	58.2	13.8	21.5	1.5
010-1	32770	3.8	0.0050	10.961	0.0012	5.770	32.2	3.5	25.2	1.5	10.35	0.0046	11.083	0.0011	7.341	29.3	3.3	21.2	1.6
019-1	58608	9.6	0.0038	15.554	0.0010	5.573	24.8	3.9	20.1	1.1	2.49	0.0038	15.778	0.0010	5.967	24.2	3.8	19.6	1.2
019-2	71304	11.7	0.0058	13.505	0.0010	5.523	37.1	5.0	20.5	1.1	3.38	0.0056	13.990	0.0010	5.721	36.3	5.1	19.8	1.1
019-3	46625	13.8	0.0068	9.452	0.0011	5.903	43.7	4.1	23.1	1.4	18.32	0.0052	10.451	0.0010	6.137	33.5	3.5	19.5	1.2
016-1	57724	35.7	0.0079	20.733	0.0010	5.628	50.5	10.5	20.4	1.1	5.15	0.0068	25.342	0.0010	5.912	43.9	11.2	20.1	1.2
002-1	16611	13.2	0.0051	6.292	0.0012	4.149	32.5	2.1	24.4	1.0	12.25	0.0041	16.184	0.0010	7.992	26.4	4.3	20.8	1.7
001-1	36158	20.2	0.0056	5.558	0.0011	3.121	35.9	2.0	22.7	0.7	6.60	0.0047	9.354	0.0011	4.388	30.1	2.8	21.4	0.9
009-1	29344	4.5	0.0032	5.217	0.0010	3.019	20.4	1.1	21.1	0.6	4.72	0.0031	6.367	0.0010	4.790	19.8	1.3	20.3	1.0

[a] Th content in ppm accurate to approximately 10%.
[b] Normalised to Th/U ratio of the standard.
[c] Percentage of ^{206}Pb that is common.
[d] Isotopic ratios are corrected for common-Pb, the common-Pb correction is based on a single stage model (Stacey and Kramers, 1975) and the interpreted age of the crystal.

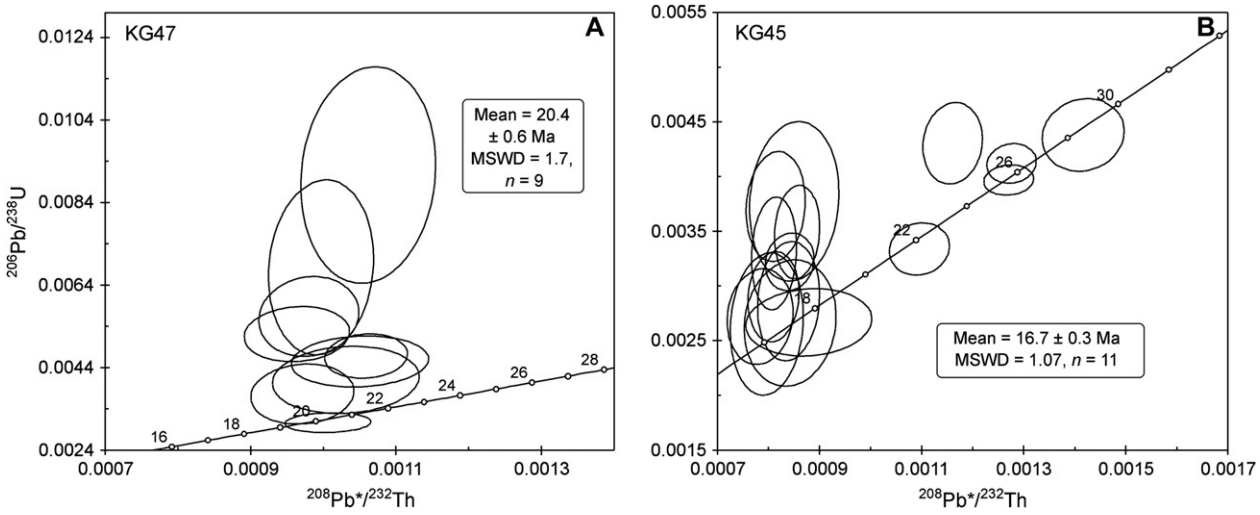

Fig. 9. Common-lead corrected $^{208}Pb/^{232}Th$–$^{206}Pb/^{238}U$ concordia plots with inverse-variance weighted mean ages for KG47 (A) and KG45 (B). Pb* refers to the radiogenic Pb: i.e. the total Pb minus common-Pb.

La region where the lower ductile detachment was active at 18–16 Ma and after 12 Ma, respectively (Hodges et al., 1998; Murphy and Harrison, 1999; Searle et al., 2003; Edwards and Harrison, 1997; Wu et al., 1998). These data suggest that there is considerable variability, both along orogenic strike and perhaps more importantly, parallel to the transport direction, in the timing and duration of slip on the STDS.

6.2. Structural evolution and exhumation

Our structural, petrological and geochronological constraints from the Dzakaa Chu section suggest that it provides a window into a deeper structural section of the STDS than exposed elsewhere in the Everest region and provides new insights into the processes involved with the early stages of south-directed exhumation of the GHS. Macro- and micro-scale structural analyses demonstrate that the discrete brittle detachment subparallel to the regional ductile fabric that is common in most parts of the orogen is not present in Dzakaa Chu section. Instead, a ~1000-m thick zone of distributed ductile shear defines the STDS. Because deformation is distributed within GHS and TSS rocks, without a discrete detachment, using footwall vs. hanging wall nomenclature is problematic and will be avoided in this discussion. To summarize our preferred interpretation for the kinematic evolution of the STDS, we propose a model, based on Jessup et al. (2006c) and inspired by the Sibson (1986) fault zone model, that combines the observations reported here with those from sections in the up tectonic transport direction (i.e., Rongbuk valley) (Fig. 10). In this model, the Dzakaa Chu area records a snap

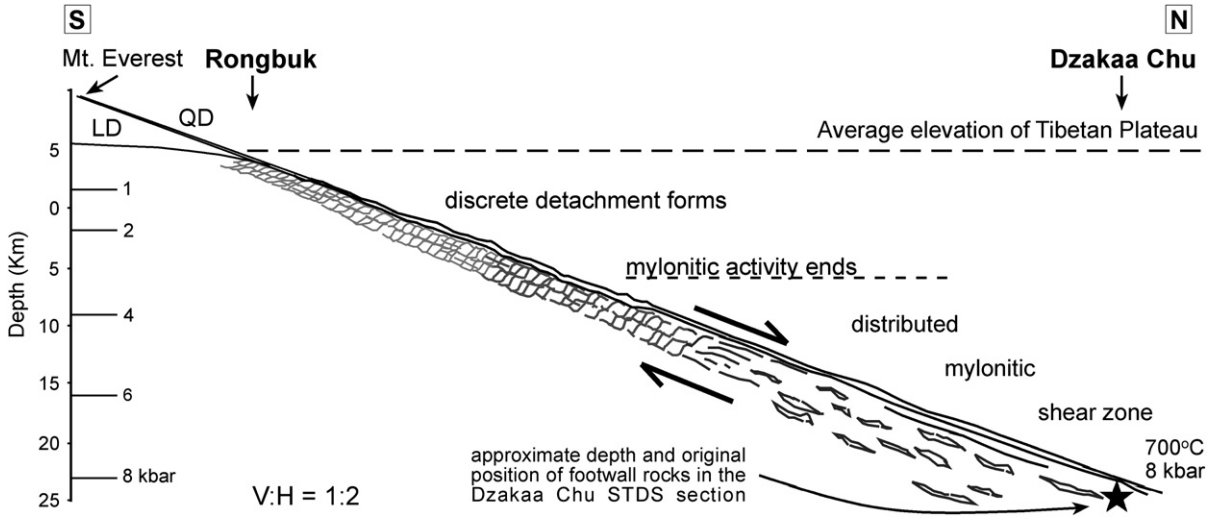

Fig. 10. Summary diagram for evolution of the STDS modified from Jessup et al. (2006b). Early ductile fabrics formed within a distributed ductile shear zone (Dzakaa Chu). As time progressed, and footwall rocks were exhumed beneath the STDS, deformation was focused into a narrower zone, with early ductile fabrics overprinted by lower temperature deformation features concomitant with formation of a discrete detachment structure(s) at high structural levels (Rongbuk valley). Thus, sections of the STDS such as Rongbuk in the Everest region are composite features containing an early ductile shear zone (LD, Lhotse detachment) that has been overprinted by a brittle detachment fault (QD, Qomolangma detachment). In contrast, the Dzakaa Chu section does not contain a brittle detachment fault and preserves only the initial ductile deformation history of the STDS system.

shot of the early stages of an evolving orogen-scale detachment (STDS) that progressed from a high-grade shear zone, where deformation temperatures exceeded those of quartz and feldspar and P–T conditions reached >700 °C and 8 kbar, into shallower crustal positions were deformation was partitioned into a 1000-m thick distributed shear zone within overlying calc-mylonites. The age of a leucogranite dyke that post-dates fabric development within the high-grade gneisses suggests that this fundamental transition had occurred by ~20 Ma in the Dzakaa Chu section. As exhumation progressed towards shallower crustal levels, mylonitic activity ceased (Fig. 10) and subsequent brittle-deformation was partitioned over a broad area in the Dzakaa Chu section. This contrasts with other sections of the STDS (e.g., Rongbuk valley; Fig. 10) where, as exhumation progressed, deformation was focused into a subparallel brittle detachment fault that juxtaposed early, strongly telescoped ductile fabrics in the footwall with hanging wall rocks (Jessup et al., 2006a).

Since the brittle features present in the Dzakaa Chu section are limited to small-scale steeply dipping brittle faults, instead of foliation-parallel detachments that are common to other sections of the STDS, we propose that the Dzakaa Chu section is representative of a deeper structural section than exposed elsewhere along the STDS, including Rongbuk valley. This implies that our results from the Dzakaa Chu section provide rare insight into the earliest stages of south-directed mid-crustal flow along the STDS that, in most areas, is overprinted by continued fabric development associated with the final stages of exhumation. For example, during the early stages of exhumation deformation was partitioned into a relatively narrow (~1 km) shear zone (STDS) along the upper margin of the GHS that accommodated ≥50 km of displacement before it progressed into a discrete detachment (Jessup et al., 2006a).

7. Conclusions

Based on detailed structural mapping, supported by petrographic and petrological data, we define the STDS in the Dzakaa Chu valley as a ~1000-m thick zone of distributed high strain separating upper amphibolite facies gneisses and leucogranites structurally below from unmetamorphosed TSS rocks structurally above. This zone spatially coincides with intensification of a mylonitic foliation and associated mineral stretching lineation in the lower part, and persistence of a cleavage in structurally higher units. In contrast to other segments of the STDS, we find no evidence for a discrete detachment fault that is subparallel to the mylonitic foliation. Instead, we interpret the Dzakaa Chu section of the STDS to represent a zone of distributed ductile deformation that accommodated ≥50 km of horizontal displacement before it was subsequently overprinted by small-scale, steeply dipping brittle features. Geochronology on leucogranites constrains ductile fabric development in the lower part of the zone to be older than ~20 Ma, indicating both significant along strike and transport parallel temporal variations of slip on the STDS. Our data suggest that the Dzakaa Chu section exposes the structurally deeper and older part of the STDS relative to other sections such as those exposed in Rongbuk valley and Dingyyê. We combine our results from Dzakaa Chu with previous kinematic and geochronological investigations to propose a model for the spatial and temporal distribution in deformation mechanisms that accommodated south-directed mid-crustal flow along the STDS. Our data from Dzakaa Chu provide important insights into the early ductile deformational mechanisms associated with this system that have elsewhere been overprinted by later-stage low-angle discrete brittle structures. This study highlights the mechanisms by which low-angle detachment fault systems accommodate ductile extension and exhumation in the mid-crust and underlines the importance of these processes with respect to understanding the tectonic evolution of not only the Himalaya but also other ancient and active contractional systems such as the Alps and the Andes.

Acknowledgements

Fieldwork was funded by NZ TEC Bright Future Top Achiever Doctoral Scholarship (TAD 1433) awarded to J.M. Cottle, a National Science Foundation grant (EAR 0207524) to R.D. Law and M.P. Searle, and a Geological Society of America research grant and a 2010 Fellowship from the College of Science at Virginia Tech to M.J. Jessup. Isotopic analyses were made possible by a Natural Environment Research Council NIGFSC grant (IP/846/0505) awarded to M.P. Searle. V. Pashley (Natural Environment Research Council National Isotope Geoscience Laboratory, Keyworth) provided considerable assistance in obtaining isotope analyses. We also thank S. Wangdue, T. Sherpa, S. Dhakal and R. Schrama for logistical support. This manuscript benefited considerably from careful and insightful reviews by Djordje Grujic and the editor Bob Holdsworth.

Appendix 1. Appendix 1U–Th–Pb analytical methods and supporting descriptions

A.1. Analytical methods

Monazites separated from a KG47 and KG45 were analysed for U–Th–Pb isotopes by Laser Ablation Multi-Collector Inductively Coupled Mass Spectrometry (LA-MC-ICPMS) at the National Isotope Geoscience Laboratories (NIGL) Keyworth using a pseudo-simultaneous multi-static acquisition method modified from Horstwood et al. (2003). Ages were calculated using the U decay constants of Jaffey et al. (1971), and the Th decay constant of Amelin and Zaitsev (2002) in Isoplot (Ludwig, 2003). Data plots were generated using Isoplot (Ludwig, 2003). All errors in data tables and concordia plots are quoted at the 2σ confidence level.

Prior to isotopic analysis, 60 (KG47) and 85 (KG45) monazite grains representing the variation in population morphology were mounted in 1 in. diameter epoxy resin discs, doubly polished and imaged in order to obtain information on zoning within grains and identify potential sub-populations of

monazite within the rocks. Backscatter electron (BSE), Th and Y maps were obtained for each grain using a Scanning Electron Microscope (SEM) or an Electron Microprobe (EMP). The BSE, Y and Th maps were also used to position analytical spots such that multiple domains were avoided where possible.

A.2. KG47 monazite chemical petrography

Monazite crystals in KG47 are generally equant, translucent green gem-quality euhedral grains ranging in size from 100 to 150 μm (long axis) (Fig. A.1A–F). Most grains have a lower-Th core (relative to the rim) that usually displays either sector (e.g., Fig. A.1E) or oscillatory zoning (e.g., Fig. A.1C). Cores are mantled by thick, but relatively homogeneous, slightly higher-Th rims (e.g., Fig. A.1A). Rims occasionally show oscillatory zoning indicative of magmatic growth zoning. Although the boundary between rim and core is generally sharp, the rims occasionally invade the cores and appear to recrystallise parts of the core.

A.3. KG45 monazite chemical petrography

Monazites separated from KG45 are clear euhedral grains ranging in size from 70 to 90 μm (long axis). BSE (Fig. A.1G–L), Y and Th imaging reveals a complex chemical petrography with the vast majority of grains showing evidence of resorption both pre- and post-rim growth. The zoning in monazites from KG45 can be grouped into two broad types. The first sub-population comprises grains with no obvious core and thick, inclusion-rich rims predominantly of quartz and K-feldspar (Fig. A.1G). These grains show several phases of resorption producing crosscutting flame-like or tongue structures. Some of these patterns may represent intergrowths of smaller grains while others are probably a result of multiple episodes of intra-crystal dissolution and re-precipitation. The second sub-population preserves oscillatory growth zoning in the inner part of the grains (Fig. A.1I). This zoning, which we interpret to be magmatic in origin is variably overprinted by re-crystallized flame-like structures, although the outline of the cores generally mimics the overall grain shape. Where possible, homogeneous areas were sampled.

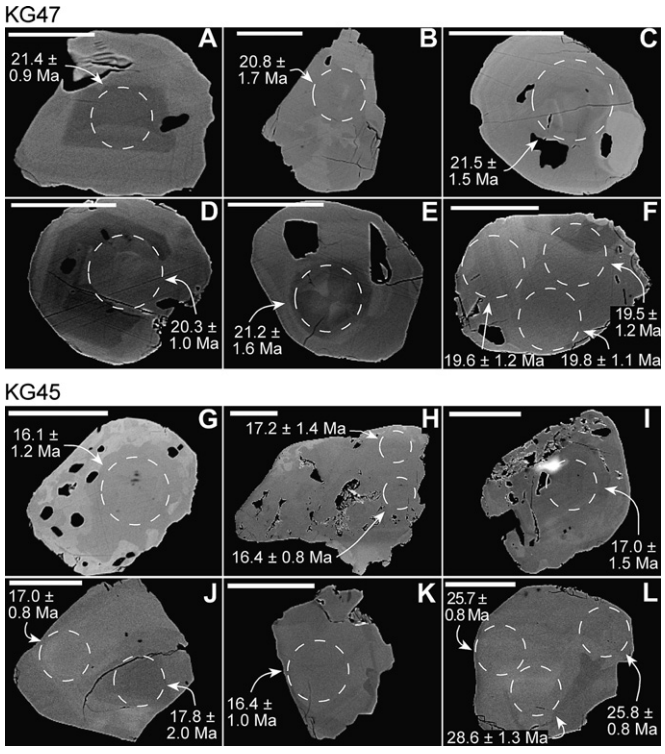

Fig. A.1. Backscatter electron (BSE) images of selected monazites analysed in this study. The lighter coloured areas are enriched in Th and U relative to the darker areas. Note that grey-scale values are not necessarily directly comparable between images. The dashed circles represent locations of 35 μm diameter spot LA-MC-ICPMS analyses. Scale bars are 50 μm. The ages refer to the $^{208}Pb^*/^{232}Th$ age ± the 2σ absolute error for each individual spot analysis; refer to Table 1 for the full analytical data set. (AF) Sample KG47 undeformed leucogranite dyke. (G–L), Sample KG45 undeformed leucogranite sill. Black inclusions in images (A), (C) (G), (I) and (K) are plagioclase, those in (E) and (D) are quartz and zircon in (F).

A.4. KG45 monazite U–Th–Pb data

Five analyses from KG45 plot on, or slightly above concordia and have ages between ~5 and 12 million years older than the main population at 16.7 ± 0.3 Ma. There are two possible explanations for these older ages. (1) They represent inheritance from up to four distinct sources, inherited from either the source and/or from wall rocks during emplacement. Alternatively, (2) these ages may represent variable mixtures of a ~17 Ma component with either the oldest measured component (~28 Ma) or an older, as yet unidentified component; i.e., the spot ages sample variable mixtures of the magmatic monazite population and inherited component(s). The main conclusion of this hypothesis is that these ages do not necessarily have any geological significance. If these ages were the result of sampling of multiple domains, it might be realistic to expect evidence of this on the time-resolved isotopic ratio measurement profiles for each spot. Careful evaluation of the profiles does not suggest any significant excess scatter over and above what would be expected for a single component within each of the analyses. In order to further assess whether these older analyses are mixed ages, we modelled the data using simple end-member mixing of a U concentration and Th/U ratio representing that of the youngest population of monazite, with a composition approximating the oldest spot analysis. The mixing curve between these two end-member compositions does not fit the data well and changing the compositions of the end-members does not improve the fit between model and data. We therefore interpret these older age components to be the result of inheritance from multiple discrete age sources. We believe that this is a plausible hypothesis given abundant evidence of inherited monazite observed in other Himalayan leucogranties (e.g. Parrish, 1990; Harrison et al., 1995) and the presence locally of multiple generations of leucogranite bodies. As with KG47, there appears to be no correlation between the chemical petrography of a grain and its age, suggesting that if any significant time gap between domains exists it is beyond the temporal resolution of our analytical technique.

References

Armijo, R., Tapponnier, P., Mercier, J.L., Tongling, H., 1986. Quaternary extension in Southern Tibet; field observations and tectonic implications. Journal of Geophysical Research 91, 13803–13872.

Amelin, Y., Zaitsev, A.N., 2002. Precise geochronology of phoscorites and carbonatites: the critical role of U-series disequilibrium in age interpretations. Geochimica et Cosmochimica Acta 66, 2399–2419.

Beaumont, C., Jamieson, R.A., Nguyen, M.H., Lee, B., 2001. Himalayan tectonics explained by extrusion of a low-viscosity crustal channel coupled to focused surface denudation. Nature 414, 738–742.

Beaumont, C., Jamieson, R.A., Nguyen, M.H., Medvedev, S., 2004. Crustal channel flows: 1. Numerical models with applications to the tectonics of the Himalayan–Tibetan orogen. Journal of Geophysical Research 109, B06406, doi:10.1029/2003JB002809.

Beaumont, C., Nguyen, M.H., Jamieson, R.A., Lee, B., 2006. Crustal flow modes in large hot orogens. In: Law, R.D., Searle, M.P., Godin, L. (Eds.), Channel Flow, Extrusion, and Exhumation in Continental Collision Zones. Geological Society, London, Special Publications, vol. 268, pp. 91–145.

Bhattacharya, A., Mohanty, L., Maji, A., Sen, S.K., Raith, M., 1992. Non-ideal mixing in the phlogopite–annite binary: constraints from experimental data on the Mg–Fe partitioning and a reformulation of the biotite-garnet thermometer. Contributions to Mineralogy and Petrology 111, 87–93.

Burchfiel, C.B., Royden, L.H., 1985. North–south extension within the convergent Himalayan region. Geology 13, 679–682.

Burchfiel, C.B., Chen, Z., Hodges, K.V., Liu, Y., Royden, L.H., Deng, C., Xu, J., 1992. The South Tibetan Detachment System, Himalayan Orogen: Extension Contemporaneous with and Parallel to Shortening in a Collisional Mountain Belt. Special Paper 269. Geological Society of America, Boulder, CO, 41 pp.

Burg, J.P., 1983. Carte Géologique du Sud du Tibet. Ministry of Geology/CNRS, Beijing/Paris.

Burg, J.P., Chen, G.M., 1984. Tectonics and structural zonation of southern Tibet, China. Nature 311, 219–223.

Burg, J.P., Brunel, M., Gapais, D., Chen, G.M., Liu, G.H., 1984. Deformation of leucogranites of the crystalline Main Central sheet in southern Tibet (China). Journal of Structural Geology 6, 535–542.

Burkhard, M., 1993. Calcite twins, their geometry, appearance and significance as stress–strain markers and indicators of tectonic regime: a review. Journal of Structural Geology 15, 351–368.

Carosi, R., Lombardo, B., Molli, G., Musumeci, G., Pertusati, P.C., 1998. The South Tibetan Detachment System in the Rongbuk valley, Everest region. Deformation and geological implications. Journal of Asian Earth Sciences 16, 299–311.

Carosi, R., Lombardo, B., Musumeci, G., Pertusati, P.C., 1999. Geology of the Higher Himalayan Crystallines in Khumbu Himal (eastern Nepal). Journal of Asian Earth Sciences 17, 785–803.

Dèzes, P.J., Vannay, J.-C., Steck, A., Bussy, F., Cosca, M., 1999. Synorogenic extension, quantitative constraints on the age and displacement of the Zanskar Shear Zone (northwest Himalaya). Geological Society of America Bulletin 111, 364–374.

Edwards, M.A., Harrison, T.M., 1997. When did the roof collapse? Late Miocene north–south extension in the high Himalaya revealed by Th–Pb monazite dating of the Khula Kangri granite. Geology 25, 543–546.

Edwards, M.A., Kidd, W.S.F., Li, J., Yue, Y., Clark, M., 1996. Multi-stage development of the southern Tibet detachment system near Khula Kangri. New data from Gonto La. Tectonophysics 260, 1–19.

Ferrill, D.A., Morris, A.P., Evans, M.A., Burkhard, M., Groshong Jr., R.H., Onasch, C.M., 2004. Calcite twin morphology: a low-temperature deformation geothermometer. Journal of Structural Geology 26, 1521–1529.

Fitzgerald, J.D., Stunitz, H., 1993. Deformation of granitoids at low metamorphic grade I: reactions and grain size reduction. Tectonophysics 221, 269–297.

Gansser, A., 1983. Geology of the Bhutan Himalaya. Birkhäuser Verlag, Basel, 181 pp.

Godin, L., 2003. Structural evolution of the Tethyan sedimentary sequence in the Annapurna area, central Nepal Himalaya. Journal of Asian Earth Sciences 22 (4), 307–328.

Godin, L., Brown, R.L., Hanmer, S., 1999. High strain zone in the hanging wall of the Annapurna detachment, central Nepal Himalaya. In: MacFarlane, A., Sorkhabi, R.B., Quade, J. (Eds.), Himalaya and Tibet: Mountain Roots to Mountain Tops. Geological Society of America Special Paper, vol. 328, pp. 199–210.

Godin, L., Parrish, R.R., Brown, R.L., Hodges, K.V., 2001. Crustal thickening leading exhumation of the Himalayan metamorphic core of central Nepal; insight from geochronology and $^{40}Ar/^{39}Ar$ thermochronology. Tectonics 20, 729–747.

Grasemann, B., Fritz, H., Vannay, J.-C., 1999. Quantitative kinematic flow analysis from the Main Central Thrust Zone (NW-Himalaya, India): implications for a decelerating strain path and the extrusion of orogenic wedges. Journal of Structural Geology 21, 837–853.

Grujic, D., Casey, M., Davidson, C., Hollister, L., Kündig, R., Pavlis, T., Schmid, S., 1996. Ductile extrusion of the Higher Himalayan Crystalline in Bhutan: evidence from quartz microfabrics. Tectonophysics 260, 21–44.

Grujic, D., Hollister, L., Parrish, R.R., 2002. Himalayan metamorphic sequence as an orogenic channel: insight from Bhutan. Earth and Planetary Science Letters 198, 177–191.

Harrison, T.M., McKeegan, K.D., Le Fort, P., 1995. Detection of inherited monazite in the Manaslu leucogranite by $^{208}Pb/^{232}Th$ ion microprobe dating: crystallization age and tectonic implications. Earth and Planetary Science Letters 133, 271–282.

Herren, E., 1987. Zanskar shear zone: northeast–southwest extension within the Higher Himalayas (Ladakh, India). Geology 15, 409–413.

Hirth, G., Tullis, J., 1992. Dislocation creep regimes in quartz aggregates. Journal of Structural Geology 14, 145–159.

Hodges, K.V., Parrish, R.R., Housh, T.B., Lux, D.R., Burchfiel, B.C., Royden, L.H., Chen, Z., 1992. Simultaneous Miocene extension and shortening in the Himalayan orogen. Science 258, 1466–1470.

Hodges, K.V., Burchfiel, B.C., Royden, L.H., Chen, Z., Liu, Y., 1993. The metamorphic signature of contemporaneous extension and shortening in the central Himalayan orogen: data from the Nyalam transect, southern Tibet. Journal of Metamorphic Geology 11, 721–737.

Hodges, K.V., Hames, W.E., Olszewski, W.J., Burchfiel, B.C., Royden, L.H., Chen, Z., 1994. Thermobarometric and $^{40}Ar/^{39}Ar$ geochronologic constraints on Eohimalayan metamorphism in the Dinggye area, southern Tibet. Contributions to Mineralogy and Petrology 117, 151–163.

Hodges, K.V., Parrish, R.R., Searle, M.P., 1996. Tectonic evolution of the central Annapurna Range, Nepalese Himalaya. Tectonics 15, 1264–1291.

Hodges, K.V., Bowring, S., Davidek, K., Hawkins, D., Krol, M., 1998. Evidence for rapid displacement on Himalayan normal faults and the importance of tectonic denudation in the evolution of mountain ranges. Geology 26, 483–486.

Horstwood, M.S.A., Foster, G.L., Parrish, R.R., Noble, S.R., Nowell, G.M., 2003. Common-Pb corrected in situ U–Pb accessory mineral geochronology by LA-MC-ICPMS. Journal of Analytical Atomic Spectrometry 18, 837–846.

Hubbard, M.S., Harrison, T.M., 1989. $^{40}Ar/^{39}Ar$ age constraints on deformation and metamorphism in the Main Central Thrust Zone and Tibetan Slab, Eastern Nepal Himalaya. Tectonics 8, 865–880.

Jaffey, A.H., Flynn, K.F., Glendenin, L.E., Bentley, C.R., Essling, A.M., 1971. Precision measurements of half-lives and specific activities of ^{235}U and ^{238}U. Physics Reviews C4, 1889–1906.

Jamieson, R.A., Beaumont, C., Nguyen, M.H., Lee, B., 2002. Interaction of metamorphism, deformation, and exhumation in large convergent orogens. Journal of Metamorphic Geology 20, 9–24.

Jamieson, R.A., Beaumont, C., Medvedev, S., Nguyen, M.H., 2004. Crustal channel flows: 2. Numerical models with implications for metamorphism in the Himalayan-Tibetan orogen. Journal of Geophysical Research 109, B06406, doi:10.1029/2003JB002811.

Jamieson, R.A., Beaumont, C., Nguyen, M.H., Grujic, D., 2006. Provenance of the Greater Himalayan Sequence and associated rocks: predictions of channel flow models. In: Law, R.D., Searle, M.P., Godin, L. (Eds.),

Channel Flow, Extrusion, and Exhumation in Continental Collision Zones. Geological Society, London, Special Publications, vol. 268, pp. 165–182.

Jessup, M.J., Searle, M.P., Tracy, R., Law, R.D., 2004. Staurolite schist marks right-way up metamorphic isograds at the top of the High Himalayan Slab, Mount Everest, Tibet/Nepal (convenors). In: Searle, M.P., Law, R.D., Godin, L. (Eds.), Programme and Abstracts for Conference on: Channel Flow, Ductile Extrusion and Exhumation of Lower-mid Crust in Continental Collision Zones. Geological Society, London.

Jessup, M.J., Searle, M.P., Tracy, R.J., Law, R.D., Cottle, J.M., Waters, D.J., 2005. Thermal–mechanical evolution of the upper-section of the Greater Himalayan Slab, Everest-Lhotse massif, Nepal. In: Abstracts with Programs, vol. 37. Geological Society of America. 388.

Jessup, M.J., Law, R.D., Searle, M.P., Hubbard, M.S., 2006a. Structural evolution and vorticity of flow during extrusion and exhumation of the Greater Himalayan Slab, Mount Everest Massif, Tibet/Nepal: implications for orogen-scale flow partitioning. In: Law, R.D., Searle, M.P., Godin, L. (Eds.), Channel Flow, Extrusion, and Exhumation in Continental Collision Zones. Geological Society, London, Special Publications, vol. 268, pp. 379–414.

Jessup, M.J., Cottle, J.M., Newell, D.L., 2006b. Exhumation of a Himalayan core complex during east–west extension enhanced by focused precipitation along the Arun River gorge; the Ama Drime Massif. Eos Transactions AGU 87 (52). Fall Meeting Supplement, Abstract T34C-03.

Jessup, M.J., Cottle, J.M., Newell, D.L., Searle, M.P., Law, R.D., Tracy, R.J., 2006c. Vorticity of flow and displacement along the South Tibetan Detachment System, Gondasampa region, Tibet. Journal of Asian Earth Sciences 26, 143.

Jessup, M.J., Searle, M.P., Cottle, J.M., Law, R.D., Newell, D.L., Tracy, R.J., Waters, D.J., P-T-t-D paths of Everest Series schist, Nepal. Journal of Metamorphic Geology, in press.

Kretz, R., 1983. Symbols for rock-forming minerals. American Mineralogist 68, 277–279.

Kündig, R., 1989. Domal structures and high-grade metamorphism in the High Himalayan crystalline, Zanskar region, Northwest Himalaya, India. Journal of Metamorphic Geology 7, 43–55.

Law, R.D., Searle, M.P., Simpson, R.L., 2004. Strain, deformation temperatures and vorticity of flow at the top of the Greater Himalayan Slab, Everest Massif, Tibet. Journal of the Geological Society, London 161, 305–320.

Ludwig, K.R., 2003. Isoplot 3.00: A Geochronological Toolkit for Microsoft Excel.

Murphy, M.A., Harrison, T.M., 1999. Relationship between leucogranites and the Qomolangma Detachment in the Rongbuk valley, south Tibet. Geology 27, 831–834.

Nelson, K.D., Zhao, W., et al., 1996. Partially molten middle crust beneath southern Tibet: synthesis of project indepth results. Science 274, 1684–1688.

Parrish, R.R., 1990. U-Pb dating of monazite and its application to geological problems. Canadian Journal of Earth Sciences 27, 1431–1450.

Powell, R., Holland, T., 1988. An internally consistent dataset with uncertainties and correlations: 3, applications to geobarometry, worked examples and a computer program. Journal of Metamorphic Geology 6, 173–204.

Robyr, M., Vannay, J.-C., Epard, J.-L., Steck, A., 2002. Thrusting, extension, and doming during the polyphase tectonometamorphic evolution of the high Himalayan crystalline zone in NW India. Journal of Asian Earth Sciences 21, 221–239.

Royden, L.H., Burchfiel, C.B., 1987. Thin-skinned N–S extension within the convergent Himalayan region: gravitational collapse of a Miocene topographic front. In: Coward, M., et al. (Eds.), Continental Extensional Tectonics. Geological Society London Special Paper, vol. 27, pp. 611–619.

Schärer, U., 1984. The effect of initial ^{230}Th disequilibrium on young U–Pb ages: the Makalu case, Himalaya. Earth and Planetary Science Letters 67, 191–204.

Searle, M.P., 1986. Structural evolution and sequence of thrusting in the High Himalayan, Tibetan-Tethys and Indus suture zones of Zanskar and Ladakh, western Himalaya. Journal of Structural Geology 8, 923–936.

Searle, M.P., 1999. Extensional and compressional faults in the Everest – Lhotse massif, Khumbu Himalaya, Nepal. Journal of Geological Society, London 156, 227–240.

Searle, M.P., Rex, A.J., 1989. Thermal model for the Zanskar Himalaya. Journal of Metamorphic Geology 7, 127–134.

Searle, M.P., Parrish, R.R., Hodges, K.V., Hurford, A., Ayres, M.W., Whitehouse, M.J., 1997. Shisha Pangma leucogranite, south Tibetan Himalaya: field relations, geochemistry, age, origin and emplacement. Journal of Geology 105, 295–317.

Searle, M.P., Simpson, R.L., Law, R.D., Waters, D.J., Parrish, R.R., 2002. Quantifying displacement on the South Tibetan detachment normal fault, Everest massif, and the timing of crustal thickening and uplift in the Himalaya and Tibet. Journal of Nepal Geological Society 26, 1–6.

Searle, M.P., Waters, D.J., Dransfield, M.W., Stephenson, B.J., Walker, C.B., Walker, J.D., Rex, D.C., 1999. Thermal and mechanical models for the structural evolution of Zanskar High Himalaya. In: MacNiocaill, C., Ryan, P.D. (Eds.), Continental Tectonics. Geological Society, London, Special Publications, vol. 164, pp. 139–156.

Searle, M.P., Simpson, R.L., Law, R.D., Parrish, R.R., Waters, D.J., 2003. The structural geometry, metamorphic and magmatic evolution of the Everest massif, High Himalaya of Nepal–South Tibet. Journal of the Geological Society 160, 345–366.

Searle, M.P., Law, R.D., Jessup, M.J., 2006. Crustal structure, restoration and evolution of the Greater Himalaya: implication for channel flow and ductile extrusion of the middle crust. In: Law, R.D., Searle, M.P., Godin, L. (Eds.), Channel Flow, Extrusion, and Exhumation in Continental Collision Zones. Geological Society, London, Special Publications, vol. 268, pp. 355–378.

Sibson, R.H., 1986. Earthquakes and rock deformation in crustal fault zones. Annual Review of Earth and Planetary Sciences 14, 149–175.

Stacey, J.S., Kramers, J.D., 1975. Approximation of terrestrial lead isotope evolution by a 2-stage model. Earth and Planetary Science Letters 26, 207–221.

Stipp, M., Stunitz, H., Heilbronner, R., Schmid, S., 2002. Dynamic recrystallization of quartz: correlation between natural and experimental conditions. In: DeMeer, S., Drury, M.R., De Bresser, J.H.P., Pennock, G.M. (Eds.), Deformation Mechanisms, Rheology and Tectonics: Current Status and Future Perspectives. Geological Society of London, Special Publications, vol. 200, pp. 171–190.

Tullis, J.A., Yund, R.A., 1992. The brittle–ductile transition in feldspar aggregates: an experimental study. In: Evans, B., Wong, T.F. (Eds.), Fault Mechanics and Transport Properties of Rocks. Academic Press, London, pp. 89–117.

Vannay, J.-C., Grasemann, B., 2001. Himalayan inverted metamorphism and syn-convergence extension as a consequence of a general shear extrusion. Geological Magazine 138, 253–376.

Walker, J.D., Martin, M.W., Bowring, S.A., Searle, M.P., Waters, D.J., Hodges, K.V., 1999. Metamorphism, melting and extension: age constraints from the high Himalayan slab of southeastern Zanskar and northwestern Lahoul. Journal of Geology 107, 473–495.

Waters, D.J., Law, R.D., Searle, M.P., Jessup, M.J., 2006. Metamorphic evolution of the upper parts of the Greater Himalayan Slab, Everest area, from the 1933 sample collection of L.R. Wager. Journal of Asian Earth Sciences 26, 143.

Wendt, I., Carl, C., 1991. The statistical distribution of the mean squared weighted deviation. Chemical Geology 86, 275–285.

Wu, C., Nelson, K.D., Wortman, G., Samson, S., Yue, Y., Li, J., Kidd, W.S.F., Edwards, M.A., 1998. Yadong cross-structure and south Tibetan detachment in the east central Himalaya (89°–90°E). Tectonics 17, 28–45.

Yin, C., Kuo, S.T., 1978. Stratigraphy of the Mount Jolmo Lungma and its north slope. Scientia Sinica 21, 629–644.

Zhang, J., Lei, G., 2007. Structure and geochronology of the southern Xainza-Dinggye rift and its relationship to the south Tibetan detachment system. Journal of Asian Earth Sciences 29, 722–736.